Academic Journal of Engineering and Technology Science
ISSN 2616-5767 Vol.9, Issue 2: 1-15, DOI: 10.25236/AJETS.2026.090201

Multi-Source Remote Sensing-Based Alteration Mineral Mapping and Exploration Potential Assessment of the Leimengou Giant Mo Deposit, Western Henan, China

Yuanye Ping[1,a], **Wei Xi**[1,b,*], **Peike Dong**[1,c]

[1]*Zhengzhou Normal University, Zhengzhou, China*
[a]*yuanyeping@126.com*, [b]*weixi@zznu.edu.cn*, [c]*235641707@qq.com*
[*]*Corresponding author*

Abstract: *The Leimengou giant molybdenum deposit, located in the Xiong'ershan district of the East Qinling metallogenic belt, represents one of the most important Dabie-type porphyry Mo systems in China. Although its magmatic evolution and ore-forming processes have been extensively studied, the district-scale distribution of alteration minerals and their structural controls remain insufficiently constrained, limiting the effectiveness of mineral exploration. In this study, we integrate multi-source remote sensing data, including Landsat-8 OLI and ZY1-02D AHSI hyperspectral imagery, to map hydrothermal alteration and assess exploration potential in the Leimengou district and its surrounding western Henan Mo belt. Landsat-derived hydroxyl, carbonate, and Fe-oxide anomalies provide the regional alteration framework, while ZY1-02D hyperspectral data allow pixel-level identification of kaolinite, sericite/illite, chlorite, montmorillonite, and K-feldspar. A fused alteration index (AI) was constructed by combining spectral indices, matched-filter results, lithological information, and structural features such as faults and ring structures. The integrated results reveal a well-defined annular alteration system around the Leimengou intrusion, with high-Fe zones coinciding with known orebodies and extending along NW–SE fault corridors. Three new high-potential exploration targets are identified. This study demonstrates the effectiveness of combining multispectral and hyperspectral remote sensing for characterizing alteration mineralogy in porphyry Mo systems and provides a transferable exploration model for the East Qinling Mo belt.*

Keywords: *Hyperspectral Remote Sensing; ZY1-02D AHSI; Landsat-8 OLI; Alteration Mineral Mapping; Porphyry Molybdenum; East Qinling Orogen; Prospectivity Analysis*

1. Introduction

The East Qinling–Dabie orogenic belt along the southern margin of the North China Craton (NCC) hosts one of the world's largest molybdenum provinces, with numerous large to giant porphyry Mo deposits distributed along several EW- to NW-trending metallogenic belts in western Henan and southern Shaanxi [1, 2]. Among these deposits, the Leimengou giant Mo system represents a typical Dabie-type porphyry deposit emplaced within Archean–Paleoproterozoic Taihua Group basement and formed during Early Cretaceous high-K calc-alkaline magmatism associated with lithospheric thinning of the NCC [3–6]. Although the geological and metallogenic evolution of Leimengou has been extensively documented—including magmatic sources, fluid evolution, and mineralization processes—several key knowledge gaps remain. In particular, the three-dimensional architecture of alteration zones, their spatial relationship to intrusive geometry, and structural controls such as ring fractures and fault intersections are still poorly constrained. These limitations hinder the integration of geological and geochemical information into district-scale exploration strategies.

Optical remote sensing offers an efficient approach to characterize hydrothermal alteration over large and complex terrains. Multispectral sensors such as Landsat have been widely employed to delineate hydroxyl, carbonate, and Fe-oxide anomalies using band ratios and Crosta-based principal component analysis [7–10]. However, multispectral data lack the spectral resolution required to discriminate specific alteration minerals. Hyperspectral sensors, including the ZY1-02D Advanced Hyperspectral Imager (AHSI), provide contiguous narrow bands across the visible to short-wave infrared (0.4–2.5 μm), enabling direct identification of key alteration minerals such as kaolinite, sericite/illite, chlorite, montmorillonite, and K-feldspar [11, 12]. Despite this advantage, applications of ZY1-02D to porphyry Mo systems remain limited.

For the Leimengou district, integrating the regional-scale capability of Landsat with the mineralogical specificity of ZY1-02D offers a unique opportunity to refine alteration mapping and improve exploration targeting. However, three major issues persist: (1) Single-sensor limitations, as existing studies rarely combine multispectral and hyperspectral advantages; (2) Weak coupling between remote sensing and metallogenic models, leading to largely qualitative interpretations; (3) Lack of an integrated multi-source remote sensing exploration framework tailored specifically to Dabie-type porphyry Mo systems. This study addresses these gaps by integrating Landsat-derived alteration anomalies with ZY1-02D hyperspectral mineral maps to construct a composite alteration framework. We further incorporate lithological, structural, and metallogenic constraints to develop a remote-sensing-based exploration model for delineating high-potential targets in the Leimengou district. The main contributions of this study include: (1) establishing a multi-source alteration mapping workflow combining Landsat and ZY1-02D; (2) integrating alteration mineralogy with geological and structural controls on Mo mineralization; (3) developing a transferable prospectivity model for porphyry Mo exploration throughout western Henan.

2. Geological setting and deposit overview

2.1. Regional Geological Framework

The Leimengou area lies within the Xiong'ershan district of the East Qinling Orogen, a major collisional belt marking the convergence between the North China Craton (NCC) and the South China Block (SCB). The region records a multistage tectonic evolution involving Paleoproterozoic basement formation, Mesozoic intracontinental orogeny, and subsequent lithospheric thinning. Collectively, these processes created a favorable geodynamic environment for large-scale porphyry molybdenum mineralization (Figure 1).

The oldest exposed rocks belong to the Archean–Paleoproterozoic Taihua Group, a metamorphic complex composed of TTG gneisses, amphibolites, and supracrustal sequences. These basement units provide a rigid structural framework for Mesozoic magmatism and serve as the primary hosts for Mo mineralization. They are unconformably overlain by Mesoproterozoic to Paleozoic sedimentary successions, including carbonates, clastic strata, and minor volcanic rocks.

During the Early Cretaceous, extensive high-K calc-alkaline magmatism was triggered by lithospheric thinning and asthenospheric upwelling along the southern margin of the NCC. This event generated widespread granitoid intrusions and Mo-enriched porphyry stocks distributed along NW–SE and EW-trending belts. The Leimengou porphyry Mo system is among the most representative products of this magmatic episode.

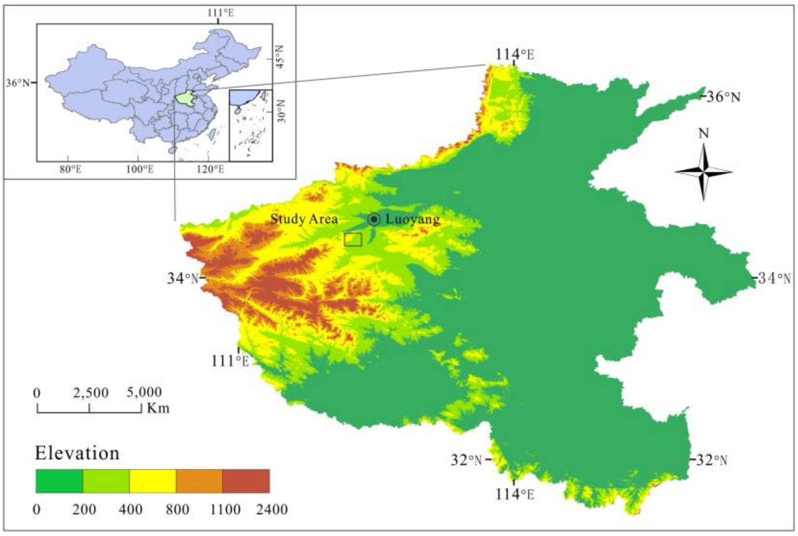

Figure 1: Location map of the study area.

2.2. Stratigraphy and Lithology of the Study Area

Regionally, the stratigraphy comprises an early Precambrian crystalline basement overlain by Mesoproterozoic–Cenozoic sequences. The basement consists mainly of Neoarchean Taihua Group high-grade metamorphic rocks, predominantly plagioclase–amphibole gneiss, amphibolite, biotite plagiogneiss, and migmatitic gneiss, representing amphibolite- to locally granulite-facies metamorphism [13, 14]. The cover sequence includes, from bottom to top, Mesoproterozoic Xiong'er Group bimodal volcanics, the Guandaokou and Luanchuan groups of mixed clastic–carbonate facies, Neoproterozoic Tonian–Sinian clastic–carbonate strata, limited Paleozoic carbonate and coal-bearing clastics, and Mesozoic redbeds overlain by Cenozoic fluvial–lacustrine deposits [1, 15].

In the immediate Leimengou area, exposed strata are relatively simple and dominated by Taihua Group gneisses and Xiong'er Group volcanics. The basement gneisses—plagioclase amphibole gneiss, biotite plagiogneiss, and amphibolite—display clear gneissic foliation trending 100–140° and dipping 15–35°, locally disrupted near intrusive contacts [16–18]. The Xiong'er Group forms a volcanic apron composed mainly of basaltic andesite, andesite, and intermediate–felsic volcanic and volcaniclastic rocks [13, 16].

Mesozoic intrusions dominate the regional magmatism. Triassic–Early Cretaceous batholiths such as the Huashan, Wancun, and Songping plutons, together with numerous porphyry stocks and dikes, define NW–SE-trending magmatic belts that coincide with major Mo–W–Au mineralization zones [1, 13]. In the Leimengou ore district, magmatic rocks include: (1) a fine- to micro-grained porphyritic monzogranite to granite porphyry intrusion (the "Leimengou intrusion"), which cuts Taihua Group gneisses and hosts the main Mo mineralization; (2) quartz porphyry dikes and small stocks that locally carry ore; and (3) an explosive breccia pipe and associated breccia bodies composed of granitoid and gneiss fragments set in a felsic matrix [3, 15–16, 18, 19].

Whole-rock geochemistry and zircon Lu–Hf isotopic data indicate that the Leimengou intrusion is peraluminous and high-K calc-alkaline, enriched in LILEs and depleted in HFSEs, with strongly negative εHf(t) values and two-stage model ages of 2.1–2.9 Ga. These signatures point to derivation predominantly from partial melting of ancient Taihua-type crust with minor mantle components [3, 5, 15].

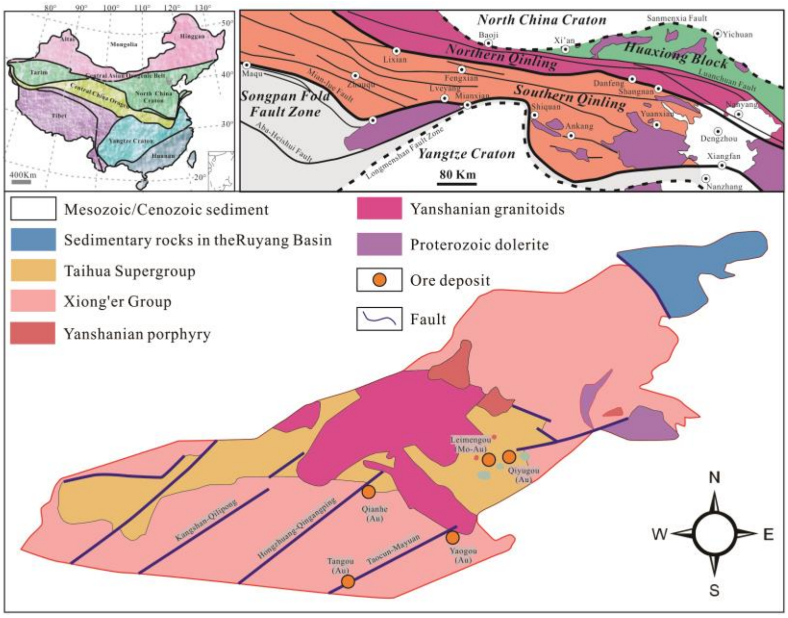

Figure 2: Simplified geological and mineral deposits map of the study area[4, 5].

2.3. Structural Framework and Ore-Controlling Factors

Regionally, the Leimengou district is situated along the Longbo–Huashan composite anticline, whose EW-trending axis is cored by Taihua Group gneisses and flanked by Xiong'er Group volcanics [8]. This fold is dissected by major EW-, NE–SW-, and NW–SE-trending faults. EW faults—including segments of the Luanchuan fault system—accommodated large-scale crustal deformation and guided the emplacement of granitoid plutons [1, 13]. NE–SW and NW–SE faults served as important secondary conduits for magma ascent and hydrothermal fluid migration [16, 19]. Within the ore field, stratigraphy, intrusions, breccia bodies, and orebodies are strongly controlled by this fold–fault architecture. The Leimengou granite stock and breccia pipe were emplaced along the southeastern limb of the anticline, where extensional–shear zones developed during Early Cretaceous lithospheric thinning [16, 19]. Remote-sensing and field observations show distinct linear and annular structures: EW lineaments correspond to the anticline axis and major faults, whereas NW–SE and NE–SW lineaments define the margins of the intrusion and breccia pipe and coincide with zones of intense alteration and mineralization [18, 19]. The No. 2 orebody lies along the inner—and more prominently the outer—contact between the porphyritic granite and the surrounding Taihua gneisses and breccia, forming a gently dipping, quasi-ring-shaped ore shell. It appears as an EW-elongated ring in plan view and as a nearly horizontal tabular body in cross-section, with a maximum thickness approaching 600 m and dips of 5–15 °[18]. Ore is concentrated within a 100–400 m halo around the intrusion and locally along the granite–breccia contact, emphasizing the role of breccia emplacement and ring fractures in channeling hydrothermal fluids [18, 19]. Thus, the major ore-controlling factors in the Leimengou district include: (1) the geometry of the granite stock and its contact relationships with the Taihua basement; (2) the presence of explosive breccia bodies and associated ring fractures; and (3) the intersection of major EW and NE–NW fault systems that enhanced permeability and localized magma emplacement, fluid flow, and ore deposition [16, 18, 19]. These structural features are consistent with the distribution of alteration halos and spectral anomalies mapped in this study.

2.4. Characteristics of the Leimengou Giant Mo Deposit

The Leimengou Mo deposit is a typical Dabie-type porphyry Mo system within the East Qinling Mo belt [1, 3, 16]. Resource estimates report (332) + (333) industrial ore reserves of 935.53 × 10^6 t with an average grade of 0.079% Mo and contained metal of 0.742 Mt, classifying it as a super-large Mo deposit. More than 90 orebodies have been identified, with the No. 2 orebody accounting for most of the resources [18]. Ores occur mainly as disseminated, veinlet, and stockwork mineralization, with minor film-like and breccia-fill textures. Molybdenite and pyrite dominate the ore mineral assemblage, with minor chalcopyrite, wolframite, galena, sphalerite, and other sulfides. Gangue minerals include quartz, K-feldspar, plagioclase, biotite, muscovite/sericite, chlorite, epidote, calcite, dolomite, fluorite, kaolinite, zeolites, and gypsum [16–18]. Hydrothermal alteration is extensive and well zoned. Major alteration types include potassic alteration (K-feldspar ± secondary biotite), silicification, sericitization/phyllic alteration, chloritization, epidotization, carbonate alteration, argillic (kaolinite-rich) alteration, and pyritization [16, 17]. Potassic alteration forms the central high-temperature core. Silicification and sericitization are intimately associated with molybdenite-bearing quartz–sulfide veins and delineate the main ore zone. Outward, chlorite–epidote–carbonate and clay-rich assemblages define a broad propylitic–argillic halo accompanied by Fe-oxide staining [16–18]. Petrographic and fluid inclusion studies distinguish four hydrothermal stages: (I) disseminated potassic alteration; (II) quartz–K-feldspar veining; (III) quartz–sulfide (molybdenite) veining; (IV) late quartz–carbonate veining [16, 17]. Stages II–III correspond to the main Mo mineralization, where silicification and sericitization overprint early potassic assemblages.

This well-defined alteration zonation, simple orebody geometry, and strong structural control provide ideal conditions for remote-sensing-based alteration mapping. Potassic, silicic–sericitic, chloritic, and carbonate–Fe-oxide assemblages correspond to diagnostic spectral signatures of K-feldspar, white mica, chlorite, carbonates, Fe oxides, and clay minerals, which can be effectively detected using Landsat-8 OLI and ZY1-02D AHSI hyperspectral data.

3. Data and preprocessing

3.1. Remote sensing datasets

3.1.1. Landsat-8 OLI/TIRS Imagery

Landsat-8 Operational Land Imager and Thermal Infrared Sensor (OLI/TIRS) Level-1 Terrain-corrected (L1T) data were used for regional alteration mapping and structural interpretation across the Leimengou district and the surrounding western Henan Mo belt. Dry-season scenes with cloud cover < 5% were selected to minimize atmospheric interference, reduce seasonal vegetation effects, and ensure radiometric consistency. All VNIR–SWIR OLI bands (30 m) were used for analysis, whereas the 15 m panchromatic band was applied solely for visual sharpening.

Multiple adjacent path/row scenes were mosaicked after rigorous radiometric and geometric consistency checks. The spectral configuration, wavelength ranges, spatial resolution, and primary geological applications of Landsat-8 OLI/TIRS are summarized in Table 1.

Table 1: Landsat 8 OLI/TIRS Sensor Parameters.

Band	**Name**	**Wavelength Range (μm)**	**Spatial Resolution (m)**	**Primary Geological Applications**
1	Coastal/Aerosol	0.433 – 0.453	30	Coastal mapping, atmospheric correction
2	Blue	0.450 – 0.515	30	Distinguishing soil from vegetation, rock types
3	Green	0.525 – 0.600	30	Assessing vegetation vigor, mapping ferric iron minerals
4	Red	0.630 – 0.680	30	Mapping iron oxides, clay, and sulfate minerals
5	NIR	0.845 – 0.885	30	Delineating vegetation, water bodies, and geological boundaries
6	SWIR 1	1.560 – 1.660	30	Identifying hydrothermal alteration (e.g., clays, micas), soil moisture
7	SWIR 2	2.100 – 2.300	30	Mapping hydroxyl-bearing minerals (e.g., alunite, kaolinite), carbonates
8	Panchromatic	0.500 – 0.680	15	Image sharpening for enhanced visual interpretation of structures
9	Cirrus	1.360 – 1.390	30	Detecting high-altitude clouds to improve data quality
10	TIRS 1	10.60 – 11.19	100 (resampled to 30)	Mapping thermal anomalies, lithological discrimination
11	TIRS 2	11.50 – 12.51	100 (resampled to 30)	Surface temperature mapping

3.1.2. ZY1-02D hyperspectral imagery

High-resolution alteration mineral mapping was conducted using ZY1-02D Advanced Hyperspectral Imager (AHSI) data. One low-cloud-cover strip fully covering the Leimengou ore district and adjacent areas was selected. The AHSI provides 166 contiguous bands spanning the visible to short-wave infrared (0.4–2.5 μm), with ~10–20 nm spectral resolution and 30 m spatial resolution, enabling detailed mineral discrimination at deposit and district scales.

Orbit geometry and swath width ensured complete and overlapping coverage, facilitating accurate co-registration with Landsat-8 scenes. Key spectral–spatial parameters and geological application foci are listed in Table 2.

Table 2: ZY1-02D (Resource Satellite-1 02D) Sensor Parameters.

Sensor	**Band Type**	**Band Number / Name**	**Spectral Range (μm)**	**Spatial Resolution (m)**	**Spectral Resolution / Notes**	**Swath Width (km)**
Advanced Hyperspectral Imager (AHSI)	VNIR	1 – 76	0.40 – 1.00	30	10 nm (Bandwidth)	60
	SWIR	77 – 166	1.00 – 2.50	30	20 nm (Bandwidth)	60
Visual and Near-Infrared Camera (VNIC)	Panchromatic	Pan	0.45 – 0.90	2.5	-	115
	Multispectral	B1 (Blue)	0.45 – 0.52	10	-	115
		B2 (Green)	0.52 – 0.60	10	-	115
		B3 (Red)	0.63 – 0.69	10	-	115
		B4 (NIR)	0.76 – 0.90	10	-	115

3.2. Preprocessing workflow

Both Landsat-8 and ZY1-02D datasets were processed following a unified workflow, including radiometric calibration, atmospheric correction, geometric correction/orthorectification, destriping/denoising, and band selection (Figure 1–Figure 3).

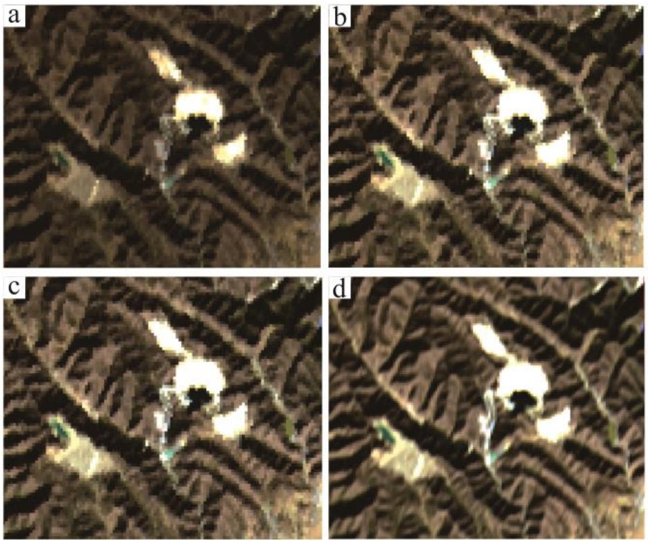

Figure 3: Remote-sensing preprocessing steps: (a) original image; (b) atmospheric correction; (c) radiometric calibration; (d) orthorectification.

Radiometric Calibration: Digital numbers were converted to at-sensor radiance using sensor-specific gains and offsets, followed by conversion to top-of-atmosphere (TOA) reflectance using solar irradiance and Sun–Earth distance corrections. For ZY1-02D AHSI, manufacturer-provided calibration coefficients were applied for each hyperspectral band.

Atmospheric Correction (FLAASH): Surface reflectance was obtained using the FLAASH atmospheric correction module. A mid-latitude atmospheric model and rural aerosol scheme were used for both datasets, with visibility determined from local meteorological conditions. Water-vapor absorption was explicitly modeled, especially for SWIR hyperspectral bands. Figure 4 shows spectral improvements after FLAASH correction.

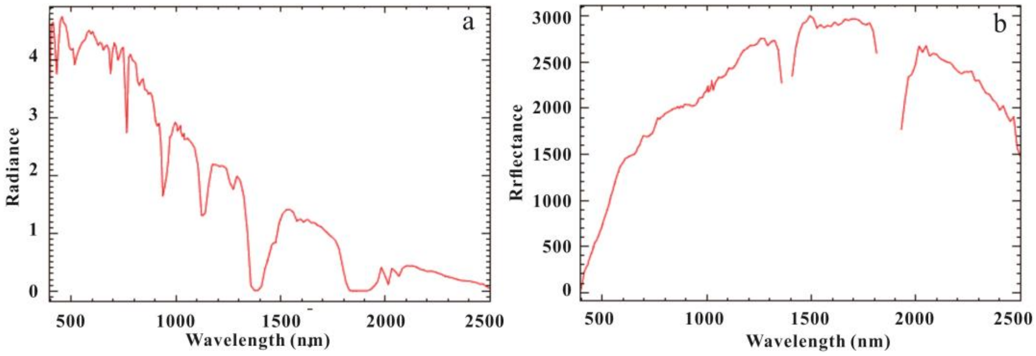

Figure 4: Remote-sensing preprocessing steps: (a) original image; (b) atmospheric correction; (c) radiometric calibration; (d) orthorectification.

Geometric Correction and Orthorectification: All imagery was orthorectified using a 30 m DEM and ground control points derived from 1:50,000 topographic maps. Landsat L1T scenes were refined via image-to-image registration, while ZY1-02D AHSI data were corrected using a rigorous sensor model combined with DEM support. The final co-registration accuracy between the two datasets is better than one pixel.

Destriping, Denoising, Band Selection, and Resampling: For ZY1-02D AHSI, residual striping and random noise were minimized using line-based destriping algorithms and a minimum noise fraction (MNF) transform. Bands heavily affected by atmospheric absorption (e.g., around 1.4 μm and 1.9 μm) and low-signal bands near the spectrum limits were removed. Landsat-8 data were destriped when necessary, and only geologically significant VNIR–SWIR bands were retained.

Because both datasets provide VNIR–SWIR bands at 30 m resolution, no additional resampling was required. All outputs were reprojected to a unified 30 m grid to ensure precise pixel-level alignment (Figure 5).

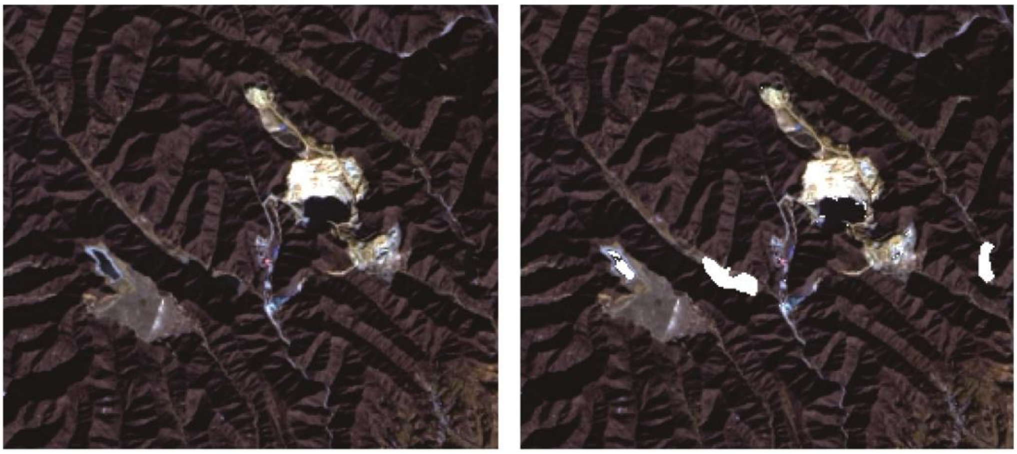

Figure 5: Comparison of original (left) and interference-removed (right) images.

3.3. Spectral library and alteration minerals

3.3.1. Standard Spectra of Alteration Minerals

A spectral library was compiled primarily from the USGS Digital Spectral Library and supplemented with published and measured mineral spectra characteristic of the East Qinling region (Figure 6). Key alteration-related minerals include: Fe-oxide/hydroxide minerals: hematite, goethite, limonite; Carbonates: calcite, dolomite, ankerite; Al- and Mg-OH-bearing clays: kaolinite, illite/sericite, montmorillonite, chlorite; Feldspars: K-feldspar (potassic alteration indicator), plagioclase.

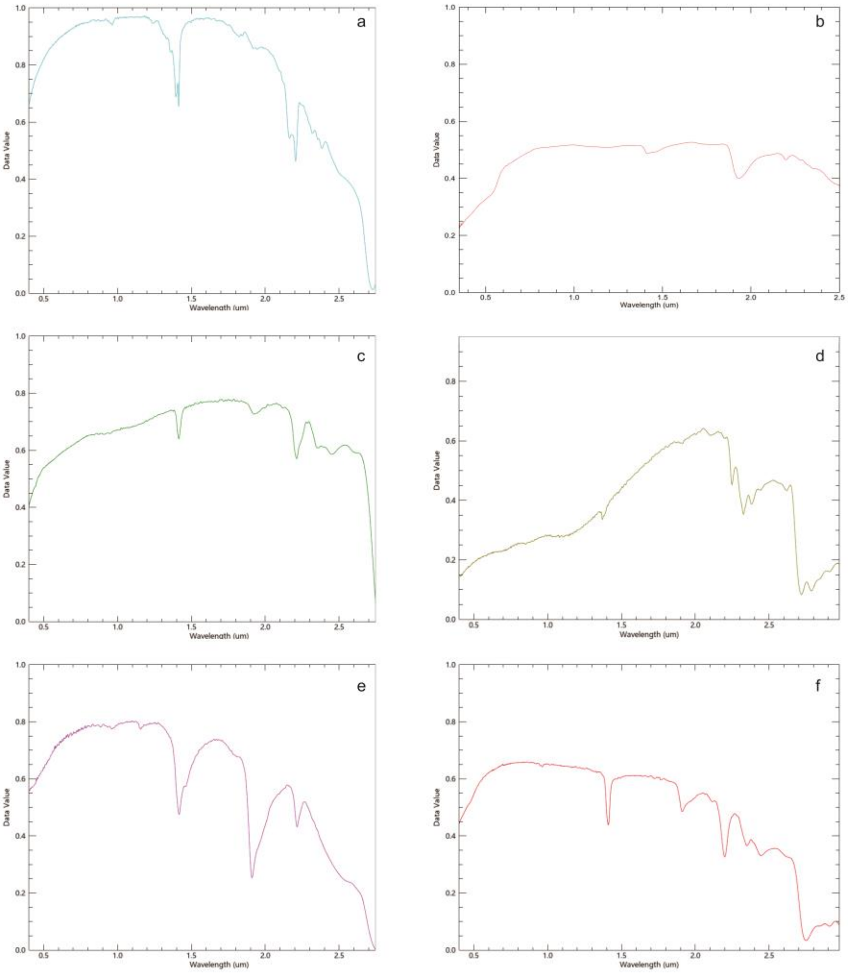

Figure 6: Representative standard spectra of major alteration minerals.

Library spectra were resampled to the spectral response functions of Landsat-8 and ZY1-02D for direct comparison and for use as endmembers in matched-filtering analysis.

3.3.2. Diagnostic absorption features

Diagnostic features in the 0.4–2.5 μm range form the foundation for alteration extraction: Fe-oxides/hydroxides: broad VNIR absorptions (0.45–0.90 μm); Carbonates: strong bands near 2.30–2.35 μm, weaker absorption at ~1.9 μm; Al-OH clays (illite/sericite, kaolinite): sharp absorptions near 2.17–2.22 μm; combination bands at ~1.4 and ~1.9 μm; Mg-OH clays (chlorite, montmorillonite): broad features near 2.30–2.35 μm extending to ~2.38–2.40 μm;K-feldspar: subtle bands in the 2.2–2.3 μm region with characteristic NIR–SWIR reflectance behavior. These features provide the spectral basis for later alteration mapping and matched-filtering procedures.

4. Remote Sensing Information Extraction

4.1. Interpretation of Lineaments and Ring Structures

Lineaments and ring/annular structures were extracted by integrating Landsat-8 OLI/TIRS, ZY1-02D AHSI, and a 30 m DEM. RGB composites and enhanced images—such as Landsat VNIR–SWIR band combinations and ZY1-02D MNF components—were generated to highlight lithologic and structural contrasts. Edge-enhancement filters (Sobel, Laplacian, gradient operators) were applied to emphasize linear features with various orientations.

Multi-azimuth hillshades (illumination from N, NE, E, SE, S, SW, W, and NW) derived from the DEM were used to enhance low-relief fault scarps and subtle circular morphologies. Candidate lineaments were semi-automatically extracted from the edge-enhanced and hillshade images, whereas ring-shaped structures were identified by detecting radial patterns and curvature anomalies. All features were subsequently refined by manual editing using geological maps and high-resolution imagery to eliminate cultural artefacts (roads, terraces) and to classify structures into major faults, subsidiary fractures, and ring/annular systems.

The final structural interpretation (Figure 7) outlines well-developed EW, NE–SW, and NW–SE fault systems, as well as multiple ring structures surrounding the Leimengou intrusion and associated explosive breccia body. These structural elements form the tectonic framework for subsequent information fusion and prospectivity modeling.

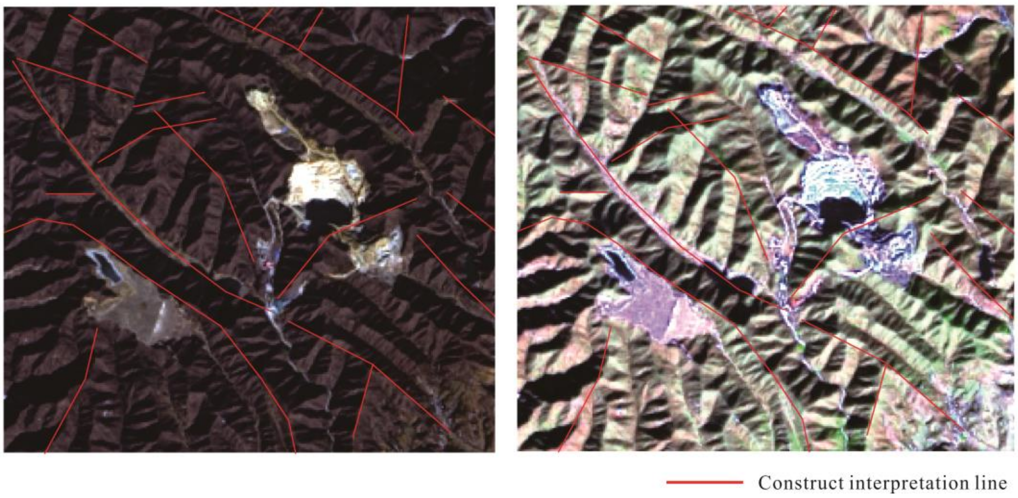

Figure 7: Structural interpretation map of the study area.

4.2. Landsat-Based Alteration Information Extraction

4.2.1. Band Selection and Spectral Indices

Landsat-8 OLI bands sensitive to iron oxides, hydroxyl-bearing minerals, and carbonates were selected to construct diagnostic spectral indices and to support Crosta-based Principal Component Analysis (PCA). The indices were defined as:

Iron-oxide index (FeI):

$$FeI = B4 / B2$$

Hydroxyl index (OHI):

$$OHI = B6 / B7$$

Carbonate index (CAI):

$$CAI = B6 / B5$$

where B2, B4, B5, B6, and B7 correspond to the Blue, Red, NIR, SWIR-1, and SWIR-2 bands, respectively.

To enhance and separate alteration signals, PCA was applied independently to the VNIR subset (B1–B4) and the SWIR subset (B5–B7). Principal components showing strong and opposite loadings on iron-sensitive visible bands or hydroxyl/carbonate-sensitive SWIR bands were selected as auxiliary anomaly layers.

4.2.2. Mapping Hydroxyl, Carbonate, and Iron-Oxide Anomalies

All spectral indices and selected PCs were normalized using min–max scaling (0–1). Anomaly thresholds were defined by combining histogram natural-breaks, cumulative probability plots, and comparisons between known mineralized and background areas. Each layer was classified into high, medium, and low anomaly zones.

Three thematic anomaly maps—hydroxyl, carbonate, and iron-oxide—were thus produced. Their spatial relationships to the Leimengou intrusion, major faults, and known orebodies are shown in Figure 8 and constitute the regional alteration framework for subsequent hyperspectral mapping and fusion.

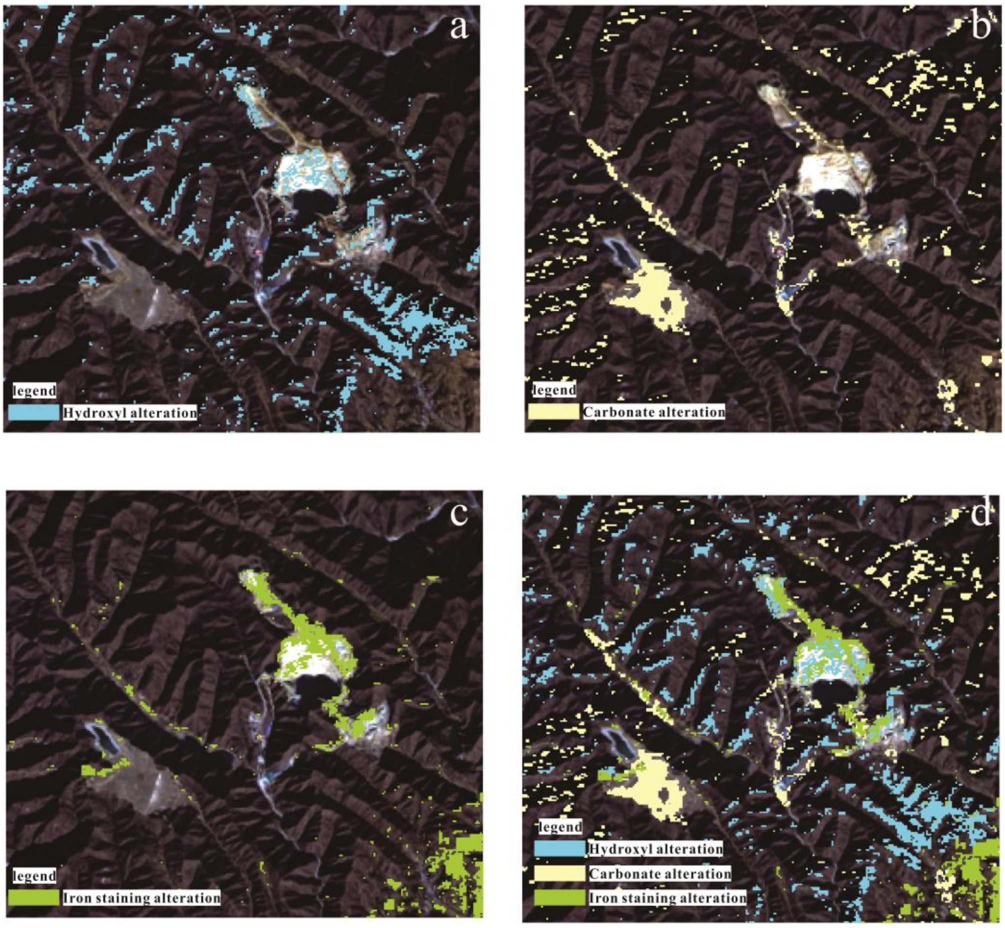

Figure 8: Regional alteration framework for hyperspectral mineral mapping and multi-source fusion.

4.3. ZY1-02D-Based Detailed Alteration Mineral Mapping

4.3.1. Dimensionality Reduction and Noise Suppression

For ZY1-02D AHSI, bands affected by strong atmospheric absorption (~1.4 and ~1.9 µm) and those with low signal-to-noise ratios at spectral extremes were removed. A Minimum Noise Fraction (MNF) transform was applied, and only MNF components exhibiting large eigenvalues and coherent geologic structure were retained.

Endmember spectra were identified using the Pixel Purity Index (PPI), n-dimensional visualization, and mineralogical knowledge of the district. Spectra extracted from ZY1-02D were compared with resampled USGS library spectra and field/laboratory spectra of kaolinite, K-feldspar, sericite/illite, chlorite, and montmorillonite. Final endmembers represented both alteration minerals and key background lithologies.

4.3.2. Matched Filtering for Alteration Minerals

Alteration minerals were mapped using the matched filtering (MF) algorithm. For each mineral—kaolinite, K-feldspar, sericite/illite, chlorite, montmorillonite, and illite—the MF was applied to MNF-reduced data using the designated endmember spectrum and the local background covariance matrix. High MF values denote stronger spectral similarity between pixels and target minerals. MF results were scaled to 0–1 and classified into high, medium, and low response classes using frequency distributions and comparisons with known mineralization. High responses delineate mineral-rich alteration centers; medium values indicate halos; low values represent background. The resulting mineral-specific distribution maps (Figure 9) reveal the detailed alteration zoning surrounding the Leimengou Mo system.

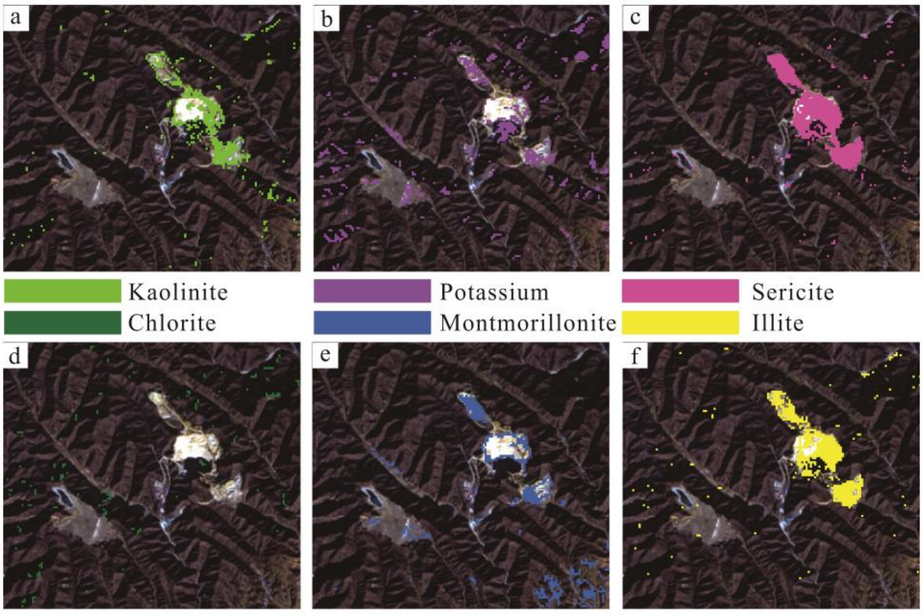

Figure 9: Alteration zonation derived from ZY1-02D matched-filtering results.

4.4. Multi-Source Fusion and Prospectivity Modeling

4.4.1. Co-Registration and Resampling

After preprocessing, Landsat-8 and ZY1-02D datasets were co-registered to a unified 30 m grid. Residual geometric offsets were corrected using tie points located at sharp lithologic boundaries and infrastructure features. Since both datasets provide 30 m VNIR–SWIR resolution, no additional spatial resampling was required; nearest-neighbor resampling was used only when necessary to preserve spectral fidelity.

4.4.2. Fusion of alteration information

All alteration layers (Landsat-derived FeI, OHI, CAI and ZY1-02D MF maps for six minerals) were normalized to 0–1. A composite alteration index (*AI*) was then computed through weighted linear overlay:

$$AI = \Sigma\, \omega_i\, A_i$$

where A_i is the *i*-th normalized layer and ω_i its weight. Higher weights were assigned to minerals and indices most diagnostic for porphyry Mo systems (e.g., K-feldspar, sericite/illite, kaolinite, Fe-oxide) and to layers showing best spatial correlation with known ore. As a sensitivity test, a fuzzy-logic combination (fuzzy OR/AND) gave similar high-AI zones and is not detailed further.

4.4.3. Remote sensing-based exploration model

A remote sensing exploration model was constructed linking: Ore-controlling factors: ore-hosting lithologies (Leimengou granite, Taihua gneiss), porphyry contacts, major faults, ring fractures; Spectral features: diagnostic Al-OH, Mg-OH, CO_3, and Fe-oxide absorptions; Image features: circular/arc-shaped halos, fault-controlled belts, intrusive textures; Exploration indicators: spatial coincidence of high AI anomalies with favorable structures and lithologies. These relationships form a “ore-controlling factor – spectral response – image expression – exploration indicator” framework (Table 3) for Mo prospecting in the Leimengou district.

Table 3: Remote sensing prospecting model for molybdenum deposits in the study area.

Factor Type	Indicator	Description (remote-sensing expression)
Ore-controlling factors	Ore-bearing lithology & structures	Granite stock, contact zones, breccia pipe, EW & NE/NW faults, ring fractures
Reflectance spectra	Spectral absorption	Strong Al-OH (~2.20 μm), Mg-OH–carbonate (~2.30–2.35 μm), Fe-oxide (0.5–0.9 μm) anomalies
Image features	Texture	Uniform fine–medium texture of intrusion relative to gneiss/volcanics
Image features	Morphology	Ring- or belt-shaped alteration around granite and breccia pipe
Image features	Linear structures & alteration pattern	NE/NW faults with inner K-feldspar–sericite–kaolinite zone and outer chlorite–montmorillonite–carbonate halo
Exploration indicators	Integrated anomaly criteria	High hydroxyl–carbonate–Fe-oxide indices coincident with strong MF responses defining Class I–II targets

4.4.4. Delineation of exploration targets

The AI map was classified into low, medium, and high classes using natural breaks. High-AI areas satisfying structural and lithologic criteria of Table 3 were merged into prospectivity domains and ranked as: Class I: high AI + optimal structural–lithologic controls; Class II: moderate AI + partially favorable conditions; Within Class I–II domains, discrete targets (T1, T2, …) were delineated by identifying local AI maxima coinciding with multiple alteration minerals and key structural intersections.

The final integrated alteration and target map provides prioritized zones for follow-up fieldwork and drilling across the Leimengou and the broader western Henan Mo belt.

5. Results and Discussion

5.1. Landsat-derived alteration anomaly patterns

The hydroxyl anomaly map displays a prominent, nearly annular high-intensity zone surrounding the Leimengou granite stock. Strong hydroxyl responses occur mainly in the southeastern and northwestern sectors, spatially coincident with the intrusive contacts, the cryptoexplosive breccia pipe, and the No. 2 orebody. Medium-intensity anomalies form diffuse halos extending outward into the Taihua Group gneisses and Xiong’er Group volcanics, particularly in the southeastern and western portions of the study area.

Carbonate anomalies are concentrated in the central, western, and northeastern regions. High-intensity carbonate responses delineate the contact zone between the granite and surrounding gneisses, as well as fracture zones developed within the Taihua basement. Several carbonate-rich linear belts follow NE–SW and NW–SE faults, indicating carbonate veining and propylitic alteration along major fluid conduits. Carbonate anomalies outside the intrusive margin appear weaker and discontinuous, reflecting reduced hydrothermal influence.

The iron-oxide anomaly map indicates that Fe-oxide staining is predominantly distributed in the central and southeastern parts of the district. Strong Fe-oxide signals occur within the upper oxidation zone and along surface-exposed fracture corridors. A well-defined Fe-oxide belt corresponds to the outcrop of the main orebody on the southeastern limb of the Longbo–Huashan anticline and continues along EW-trending faults. Additional Fe-oxide anomalies appear around the breccia pipe margin and along several NE–SW structures, marking oxidized sulfide zones and near-surface expressions of hydrothermal alteration.

5.2. ZY1-02D-derived alteration mineral distributions

Matched-filtering results from ZY1-02D reveal that kaolinite and sericite/illite form a distinct ring- to belt-shaped zone around the granite stock and breccia pipe. This kaolinite–sericite halo is narrow in the north but thickens toward the southeast and southwest, corresponding to the main ore-bearing sectors. These patterns reflect the development of medium- to high-temperature phyllic and argillic alteration superimposed on the potassic core.

Chlorite and montmorillonite define more distal, lower-temperature alteration zones. High chlorite responses are mainly distributed in the outer Taihua gneiss envelope and along several NE–SW and NW–SE faults, whereas montmorillonite appears in fragmented peripheral areas affected by stronger weathering. Together, they outline an external propylitic–argillic halo surrounding the sericite–kaolinite zone and extending along major structures west and northeast of the intrusion.

K-feldspar anomalies are tightly concentrated within the Leimengou granite and along its contact zones. The strongest responses cluster within the central portion of the granite stock and around the breccia pipe, corresponding to the potassic alteration core documented by petrographic and fluid inclusion studies. Moderate K-feldspar enrichment occurs along the ring-shaped No. 2 orebody and along EW-trending fractures crossing the intrusion, consistent with the geometry of the potassic core and its spatial linkage to mineralization. The spatial distribution of these minerals is shown in Figure 9.

5.3. Integrated Alteration Map

The fused alteration map (Figure 10)—combining Landsat-based hydroxyl, carbonate, and Fe-oxide indices with ZY1-02D kaolinite, K-feldspar, sericite/illite, chlorite, and montmorillonite layers—reveals several district-scale patterns.

A prominent quasi-ring-shaped zone of high composite alteration index (AI) surrounds the granite stock and breccia pipe. This zone corresponds to the principal potassic–phyllic–argillic alteration belt, enclosing the No. 2 orebody. Local AI maxima occur within the ring and coincide with outcrops and known subsurface extensions of mineralization.

Outside the main ring, secondary belts of elevated AI extend along NW–SE faults to the west and northeast of the intrusion. These belts represent overlapping hydroxyl, carbonate, chlorite, and Fe-oxide anomalies, accompanied by moderate kaolinite and sericite responses. Low-AI areas correspond to unaltered or weakly altered Xiong’er volcanics and distal Taihua gneisses. Overall, the AI distribution correlates strongly with known mineralized zones and provides a coherent district-scale representation of alteration intensity.

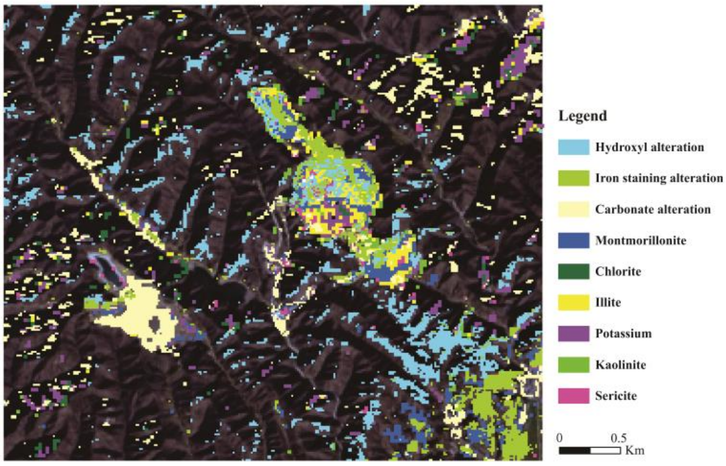

Figure 10: Fused alteration map of the study area.

5.4. Prospectivity Zoning and Target Delineation

Based on the composite alteration index and the remote sensing exploration model, the study area was subdivided into three prospectivity classes. Class I (high potential) zones comprise areas with high AI values that also coincide with favorable ore-controlling factors, including the contact between the Leimengou granite and Taihua gneisses, ring/annular structures around the breccia pipe, and intersections of NE–NW faults. These zones encompass the known Leimengou orebodies and extend westward and northeastward along major structural corridors. Class II (moderate potential) zones exhibit moderate AI but favorable lithologic or structural conditions, particularly along NE–SW faults cutting the Taihua basement and Xiong’er volcanics northwest and southeast of the main deposit. The spatial distribution of these zones is shown in the prospectivity map (Figure 11).

Within the Class I–II domains, several discrete exploration targets (Target 1, Target 2, …) were delineated based on local AI maxima and the superposition of potassic (K-feldspar), phyllic (sericite/illite), argillic (kaolinite), and Fe-oxide anomalies with ring/linear structures and intrusive contacts. Target Area 1 corresponds to the known orebody located at and near the contact zone between the granite and surrounding lithologies, situated southwest of the main mineralized center. Target Area 2 includes two localities in the northwest and southeast of the main orebody, extending along a NW–SE fault zone and characterized by strong, overlapping anomalies of kaolinite, sericite, and iron oxide.

Comparison with previous exploration (surface workings, trenches, and limited drilling) indicates that most known mineralized points fall within Class I zones and within or adjacent to delineated targets, providing first-order validation of the prospectivity model. Several newly identified targets lie in areas with little or no drilling, highlighting priority sectors for future field validation and combined geophysical–geochemical surveys.

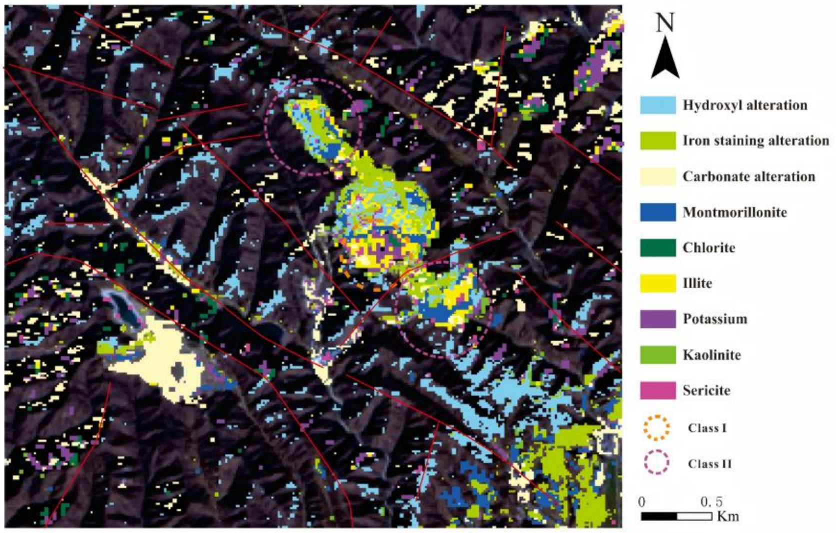

Figure 11: Prospectivity map showing fused alteration anomalies and exploration targets.

6. Conclusion

This study integrated multispectral (Landsat-8 OLI) and hyperspectral (ZY1-02D AHSI) remote sensing data with structural and lithological information to characterize alteration zoning and delineate exploration targets in the Leimengou Mo deposit and its surrounding district. The main conclusions are as follows: (1) Landsat-derived spectral anomalies effectively outline district-scale hydrothermal alteration. Hydroxyl, carbonate, and Fe-oxide indices reveal a quasi-annular alteration system centered on the Leimengou granite stock and breccia pipe. Hydroxyl anomalies delineate phyllic–argillic alteration around intrusion margins, carbonate anomalies trace propylitic alteration along major NE–SW and NW–SE faults, and Fe-oxide anomalies highlight oxidation zones linked to near-surface sulfide mineralization. These patterns demonstrate the utility of Landsat indices for identifying large-scale alteration halos and structural fluid pathways. (2) ZY1-02D hyperspectral data provide high-resolution maps of key alteration minerals. Matched-filtering results show that kaolinite, sericite/illite, and K-feldspar form well-organized alteration zonation: an inner potassic core (K-feldspar), a phyllic–argillic ring (sericite/illite, kaolinite), and an outer propylitic halo (chlorite, montmorillonite). These spatial patterns correspond closely with known ore-bearing sectors and confirm the typical zonation of porphyry-type hydrothermal systems. (3) The fused alteration index (AI) successfully captures the integrated hydrothermal footprint of the deposit. Combining multispectral and hyperspectral layers produces a comprehensive alteration map that delineates a strong ring-shaped high-AI zone around the granite stock. Secondary high-AI belts follow NW–SE faults to the west and northeast. The AI distribution correlates strongly with known orebodies, validating the fusion approach and demonstrating the advantage of integrating multi-source remote sensing data. (4) Prospectivity zoning highlights several high-potential sectors for further exploration. Class I zones—characterized by high AI and favorable ore-controlling structures such as intrusive contacts, ring fractures, and fault intersections—encompass all known orebodies and extend into areas with limited previous drilling. Class II zones mark additional structurally favorable belts with moderate alteration intensity. Within these zones, several discrete targets were delineated, including two untested sectors with strong overlapping anomalies of kaolinite, sericite/illite, and Fe-oxide. (5) Remote sensing provides an efficient framework for regional exploration in the western Henan Mo belt. The integrated approach demonstrates that combining Landsat- and hyperspectral-derived alteration information with structural interpretation can reliably identify mineralized zones and guide field exploration. The newly delineated targets provide prioritized areas for detailed geological mapping, geophysical surveys, and drilling.

Acknowledgements

Funding: Henan Provincial Science and Technology Department's Science and Technology Key Project (Project No. 252102320324); Henan Provincial Science and Technology Department's International Scientific and Technological Cooperation Project (252102520033).

References

[1] Mao, J.W., Pirajno, F., Xiang, J.F., et al. Mesozoic molybdenum deposits in the East Qinling–Dabie orogenic belt: Characteristics and tectonic settings. Ore Geology Reviews, 2011, 43: 264-293.
[2] Chen, Y.J., Pirajno, F., Li, N., et al. Geology and Geochemistry of Molybdenum Deposits in the Qinling Orogen, China. Springer, Singapore, 2022.
[3] Cao, J., Ye, H., Chen, X., et al. Geochemistry, zircon U–Pb age, and Lu–Hf isotope of the granite porphyry in Leimengou Mo deposit, East Qinling molybdenum ore belt, China. Minerals, 2018, 8: 293.
[4] Qi, N., Wang, P., et al. The geochronology, geochemistry and petrogenesis of the Leimengou porphyries, Qinling Orogen, central China. Ore Geology Reviews, 2023, 152: 105281.
[5] Qi, N., Yu, J., Dong, Y.P., et al. Fluid inclusion and He–Ar–Pb isotope studies of the Dabie-type Leimengou giant porphyry Mo deposit, Qinling Orogen. Ore Geology Reviews, 2024, 171: 106153.
[6] Tang, L., Hu, X., Chen, Y.J., et al. Fluid inclusion evidence for magmatic–hydrothermal evolution of closely linked porphyry Au, porphyry Mo and barren systems, East Qinling, China. GSA Bulletin, 2022, 134: 1529-1549.
[7] Sabins, F.F. Remote sensing for mineral exploration. Ore Geology Reviews, 1999, 14: 157-183.
[8] Pour, A.B., Hashim, M. The application of ASTER remote sensing data to porphyry copper and epithermal gold deposits. Ore Geology Reviews, 2012, 44: 1-9.
[9] Cudahy, T. Hyperspectral remote sensing in lithological and mineral mapping: A review. Journal of Applied Remote Sensing, 2021, 15: 031501.
[10] Pour, A.B., Hashim, M. Hydrothermal alteration mapping from Landsat-8 data, Sar Cheshmeh copper mining district, Iran. Journal of Taibah University for Science, 2015, 9: 155-166.
[11] Chen, L., Sui, X., Liu, R., et al. Mapping alteration minerals using ZY1-02D hyperspectral data in coalbed methane enrichment areas, NE Ordos Basin, China. Remote Sensing, 2023, 15: 3590.
[12] Tang, H., Zhang, H., Hui, C. Validation of ZY1-02D satellite sensor on-orbit radiometric calibration accuracy. In: CHREOC 2022, Lecture Notes in Electrical Engineering, 2023, 969: 649-666.
[13] He, D.Y., Qiu, K.F., Yu, H.C., et al. Lithospheric architecture and evolution of the Qinling Orogen of Central China and associated controls on metallogeny. Earth-Science Reviews, 2025: 105092.
[14] Li, Y.F., Mao, J.W., Liu, D.Y., et al. SHRIMP zircon U–Pb and molybdenite Re–Os datings for the Leimengou porphyry molybdenum deposit, western Henan and its geological implication. Geological Review, 2006, 52: 122-131.
[15] Qi, N., Holtz, F., Derrey, I.T., et al. Petrogenesis of syn-ore granites and implications for the Leimengou porphyry molybdenum deposit, Qinling Orogen, central China. Ore Geology Reviews, 2023, 163: 105781.
[16] Chen, X.D. Fluid Metallogenic Processes of the Leimengou Porphyry Molybdenum Deposit in

Western Henan, China. Master's Thesis, China University of Geosciences (Beijing), 2012.
[17] Chen, X.D., Ye, H.S., Mao, J.W., et al. Ore-forming fluid characteristics and geological significance of the Leimengou porphyry Mo deposit, western Henan. Acta Geologica Sinica, 2011, 85: 1629-1643.
[18] Sun, F.J., Liu, Y., Zhou, Y.F., et al. Research on metallogenic geology and geochemical environment of Leimengou mining area, Songxian County of Henan Province. World Nonferrous Metals, 2020(10B): 97-102.
[19] Zhang, C.F., Zhou, B.L., Xia, M.Z., et al. Geochemical characteristics and geological significance of cryptoexplosive breccia in the western segment of the Leimengou Mo ore district, western Henan. Acta Petrologica Sinica, 2021, 37: 2910-2922.